ISSN 0038-0946, Solar System Research, 2018, Vol. 52, No. 2, pp. 153–167. © Pleiades Publishing, Inc., 2018.
Original Russian Text © L.I. Shestakova, B.I. Demchenko, 2018, published in Astronomicheskii Vestnik, 2018, Vol. 52, No. 2, pp. 168–182.

Orbital Evolution of Dust Particles in the Sublimation Zone near the Sun

L. I. Shestakova* and B. I. Demchenko

Fesenkov Astrophysical Institute, Almaty, 050020 Kazakhstan

**e-mail: shest1952@mail.ru*

Received March 17, 2017

Abstract—We have performed the calculations of the orbital evolution of dust particles from volcanic glass (*p*-obsidian), basalt, astrosilicate, olivine, and pyroxene in the sublimation zone near the Sun. The sublimation (evaporation) rate is determined by the temperature of dust particles depending on their radius, material, and distance to the Sun. All practically important parameters that characterize the interaction of spherical dust particles with the radiation are calculated using the Mie theory. The influence of radiation and solar wind pressure, as well as the Poynting–Robertson drag force effects on the dust dynamics, are also taken into account. According to the observations (Shestakova and Demchenko, 2016), the boundary of the dust-free zone is 7.0–7.6 solar radii for standard particles of the zodiacal cloud and 9.1–9.2 solar radii for cometary particles. The closest agreement is obtained for basalt particles and certain kinds of olivine, pyroxene, and volcanic glass.

Keywords: F-corona, near-solar dust, sublimation (evaporation), zodiacal cloud, dust dynamics

DOI: 10.1134/S0038094618010082

INTRODUCTION

The zone of dust sublimation near the Sun is the place where many key processes occur that are associated with the interaction and exchange of matter between the solar corona and surrounding zodiacal dust cloud, as well as Sun-approaching comets. This region has so far been inaccessible for full-scale observations due to the proximity of the bright solar disk. The ground-based observations of this region, the so-called dust corona, or F-corona, are scarce, since they are only possible during total solar eclipses, when the Earth's sky background is significantly fainter. A difficulty with observations is also associated with the fact that, starting from the distances of 4 solar radii (R_s), the sky brightness during the eclipse exceeds the brightness of the dust corona. Nonetheless, such studies are possible in principle, if special spectral observation equipment is used (Beavers and Eitter, 2009; Shestakova and Demchenko, 2016).

The classical observations of the F-corona in the visible region to large distances (Blackwell, 1955) show close agreement with the Ingham model (1961), from which the radii of the sunlight-scattering dust particles are obtained: $s = 0.3$ μm. However, the numerical modeling and direct spatial measurements of zodiacal light showed that the particle radii should be in the interval of 10–100 μm (Leinert, 1975).

In the second half of the 20th century, aside from the optical observations, observations of the dust corona in the IR range were performed, both ground-based and onboard the *Concorde 001* supersonic aircraft (Lena et al., 1974). These observations made it possible to discover the regions of increased dust concentration at certain distances from the Sun. The observations by Lena et al. (1974) in the mid-IR range at $\lambda = 8–13$ μm showed an overall high level of intensity, which was significantly higher than in the near-IR range. This fact was explained by the excess concentration of small silicate particles in the F-corona.

Using the COBE/DIRBE space experiments in the IR range, the structure of the interplanetary dust cloud was studied and its model was obtained (Reach et al., 1997; Kelsall et al., 1998).

These observations were targeted toward studying the faint sky background at large distances from the Sun. The sublimation zone is still not well-studied, despite the increasing number of various space missions. Scientists turned their attention to the sublimation zone after Peterson (1967) and MacQueen (1968) reported on discovering the local maxima of the thermal emission of dust in the F-corona at wavelengths of 2.2 and 3.5 μm at heliocentric distances 3.4, 4.0, 8.7, and 9.2 R_s. Later studies with the model simulations explaining these results (Kaiser, 1970) stimulated further research in this area.

Our studies of the distribution of the radial velocity of dust in the near-solar region have extended over several decades, since they are associated with the observations of total solar eclipses in field conditions. During the eclipse of July 31, 1981, in northern

Kazakhstan, the first observations of the two-dimensional field of radial velocities of dust were performed at elongations from 3 to 7 R_s using the Fraunhofer lines near the Mg I triplet, i.e., approximately $\lambda = 5200$ Å (Shcheglov et al., 1987; Shestakova, 1987). The results of the observations allowed us to assume the existence of the boundary of the dust-free zone at a distance of approximately 6.5 R_s for the undisturbed outer zone, where the concentration of particles varies as $n(r) \propto n_0 (R/R_0)^{-1.1}$. The average particle radius that satisfies the observations is $s = 0.4$ μm.

The appearance of new data on the refractive indices of various materials in a large interval of wavelengths made it possible to calculate the emission spectra of these materials for various temperatures (T_g) and particle sizes (s) using the Mie theory. The temperature distributions of dust particles were calculated using the data on the energy distribution in the solar spectrum (Roser and Staude, 1978). The solution of this problem was significantly contributed by the numerical calculations of the orbital evolution of dust particles in the sublimation zone (Lamy, 1974a; 1979b; Mukai et al., 1974; Mukai and Yamamoto, 1979). The reviews by Burns et al. (1979) and Shestakova and Tambovtseva (1995) summarized the results of the studies of dust particle dynamics. These authors analyzed various aspects of the influence of the radiation pressure on small particles in the Solar System. All papers related to the problem of the orbital motion of dust particles, starting with (Belton, 1966), point to a region where the particles stop spiraling in toward the Sun (in agreement with the Poynting–Robertson law) and begin to move outward. The concentration of particles rises in such regions. Therefore, it is natural to conclude that the regions of particle concentration should coincide with the thermal emission maxima observed in the F-corona. In this case, the problem of modeling is reduced to selecting the suitable kind of particles, whose concentration region, which is obtained from the orbital evolution calculations, will coincide with the position of the observed thermal emission maxima. To a certain degree, this goal was achieved in (Shestakova and Tambovtseva, 1995).

However, the situation turned out to be more complex. During the total solar eclipse of July 11, 1991, no excess radiation was detected in the wavelength range between 1.2 and 2.24 μm at distances from 3 to 15 R_s (Hodapp et al., 1992; Lamy et al., 1992; Mann and MacQueen, 1993).

In our observations (Shestakova and Demchenko, 2016), we used special spectral equipment which made it possible to distinguish the contribution of the F-corona in the line of sight. The joint expedition, which included scientists from the Sternberg Astronomical Institute of Moscow State University (Moscow) and Fesenkov Astrophysical Institute (Alma-Ata), was located in northern Kazakhstan, in the settlement of Shortandy of Tselinograd oblast. As a result, it was shown that detailed spectral observations of the dust corona to large distances from the Sun on the order of 7R_s were possible. On July 11, 1991, in Mexico, a second attempt was made to obtain the boundary of the dust-free zone from direct observations. This attempt was less successful, as it was not possible to access the deeper zone of the outer corona (Aimanov et al., 1995).

After a long pause, we again successfully observed the field of radial velocities of dust in the F-corona. The observations were carried out under fine weather conditions in Kazakhstan, near the settlement of Mugalzhar in Aktyubinsk oblast during the total solar eclipse of March 29, 2006 (Shestakova et al., 2007). The observations were repeated in a short interval, since the shadow zone of the eclipse of August 1, 2008, was also close to our region. The observations were performed in Russia, near the city of Barnaul, using nearly the same equipment (Shestakova et al., 2009), the basis of which was developed for the eclipse of 1991. Only the interference filters and radiation receiver (the Apogee Alta-10 CCD camera) were chosen anew.

The results of observations of the eclipses on July 31, 1981, August 11, 1991, and August 1, 2008, revealed an east–west asymmetry in the sign of radial velocities: they were negative to the east of the Sun and positive to the west. This velocity distribution indicates the near-ecliptic orbital motion of dust coinciding with the direction of planetary motion.

During the eclipse of March 29, 2006, the dynamic connection with the zodiacal cloud was found to be nearly absent. At the same time, the direction was determined, in which the observed velocities are the highest by value and opposite by sign at the opposite sides of the Sun; this indicates the presence of the orbital motion that deviates from the ecliptic plane. The results of 2006 (Shestakova et al., 2007; Shestakova and Demchenko, 2016) show a clear genetic connection of the observed orbital motion of dust with the parent comets of the Kreutz family that were detected near the Sun close to the eclipse date.

The values of the velocities observed near the symmetry line in the plane of the sky rise with increasing elongation, which is possible if the line of sight crosses an empty dustless zone. The modeling of the observational data close to the symmetry plane allowed us to obtain the parameters of dust distribution near the sublimation zone.

In 2006, the "black" cometary dust with a low albedo ($A = 0.05$) was observed (Shestakova and Demchenko, 2016); it showed high values of the power-law exponents in the distribution of dust concentration with distance ($\nu = 2.2 > 1$) and in the size distribution of particles ($\gamma = 5.2 > 4.0$), as well as a strong radiation pressure ($\beta = 0.70–0.74$). The average radius of particles ($s \approx 0.8–0.9$ μm) and the radius of the dust-free zone ($R_o \approx 9.1–9.2$ R_s) were determined;

the latter corresponds to the distances of disintegration of low-melting point components of olivines and pyroxenes.

In 2008, the zodiacal dust was observed that concentrated toward the ecliptic plane (Shestakova and Demchenko, 2016); it demonstrated the classical parameters: $A = 0.1–0.2$, $\nu \approx 1$, $\beta \approx 0$, $\gamma = 4.0$, the average radius of the particles $s \approx 0.9–1.2$ μm, and the radius of the dust-free zone $R_o \approx 7.0–7.6\ R_s$.

The results of the observations allow revising various minerals and rocks, in order to find the materials whose sublimation zone coincides with these observations.

The present paper is dedicated to studying the orbital evolution of dust particles of various chemical composition, from semitransparent volcanic glass (p-obsidian) to strongly absorbing olivine. We have considered the temperature balance and dynamics of dust particles in the sublimation zone near the Sun using the data on refractive indices of all materials. The objective of the study is to select the materials that match the observational results (Shestakova and Demchenko, 2016) most closely.

INITIAL DATA

The orbital evolution was calculated taking into account the evaporation of dust particles. The sublimation rate depends on the heating temperature of the dust particles, as well as on their radius, constituent material, and distance from the Sun.

The influence of the radiation pressure, solar wind pressure, and Poynting–Robertson deceleration effects were also considered. It is assumed that the dust particles are heated isothermally and sublimate isotropically; the reactive forces are absent. Additionally, the influence of the planets and collisions between the particles are neglected, and the particles are considered electrically neutral. It is assumed that the dust particles have a spherical shape and homogeneous composition. The range of particle radii (s) from 0.01 to 100 μm was analyzed.

All practically important parameters, which characterize the interaction of spherical dust particles with the radiation, are calculated by the Mie theory (Boren and Hafmen, 1983; Masafumi and Munezo, 1985).

The parameters n and k are the input parameters of the Mie theory; they depend on the wavelength λ and type of matter and are specified in a tabular form for each substance separately. The Mie theory widely uses the algebra of complex numbers. However, all practically important parameters that characterize the interaction of the dust particles with the radiation, including the efficiency factors of absorption (Q_{abs}) and radiation pressure (Q_{pre}) have real values.

The selected substances (p-obsidian, basalt, astrosilicate, olivine, and pyroxene) have different properties of absorption of solar radiation. The p-obsidian substance is the droplets of semitransparent volcanic glass, which is poor in iron and weakly absorbs the solar radiation. The pyroxene $MgSiO_3$ with 100% content of magnesium and zero content of iron absorbs the solar radiation even more weakly; its particles barely evaporate until the encounter with the Sun. The particles of the synthetic substance olivine with the formula $MgFeSiO_4$ and astrosilicate, on the contrary, are rapidly heated and evaporate far from the Sun. Basalt and intermediate variations of olivine and pyroxene with 50% content of iron and magnesium with the formula $MgFeSiO_3$, as will be shown below, evaporate in the zone that is in a better agreement with our observations.

The initial data on the energy distribution in the solar spectrum are cited from various tables of the book by Makarova et al. (1991). We used the data for the wavelength range from $\lambda_1 = 0.0075$ to $\lambda_2 = 50$ μm, preliminarily converting the data into a unified system of units. For the same range, we also used the tables of complex refractive indices for all materials under study: $m(\lambda) = n(\lambda) + ik(\lambda)$, with the addition of extrapolated values from the UV range. The measurement data on the refractive indices of p-obsidian and basalt are cited from Lamy (1978) and Pollack et al. (1973); the calculations for the artificial substance astrosilicate, from Draine (1985); and the synthetic data for minerals and their combinations (olivine and pyroxene with various content of iron and magnesium), from the tables by Dorschner et al. (1995). According to our estimates, the contribution of the two unaccounted intervals $(0, \lambda_1)$ and (λ_2, ∞) in all practically important cases is less than 2%. The parameters of the materials and constants for calculating the evaporation of particles are summarized in Table 1. The sublimation rate is calculated according to Lamy (1974b) for silicates.

The typical parameters of solar wind are taken in accordance with the two-fluid model, obtained from the results of long-term observations (Veselovskii, 2007) in the interval of distances between 2 and 270 R_s, considering the radial and tangential components of the solar wind velocity. The solar wind is considered isothermal and radial, with the mass loss rate $\dot{M}_S = 2\times10^{-14}\ M_s$ (solar masses) per year and velocity at the Earth's orbit of approximately 400 km/s. The region of the solar wind corotation is within 10 R_s. The starting conditions are specified separately: the particles either move autonomously with circular orbital velocity, or escape the parent bodies (comets) with a parabolic velocity. All calculations are performed by means of our own computer codes after thorough verification using the known published examples of calculations (Boren and Hafmen, 1983; Masafumi and Munezo, 1985).

Table 1. Properties of materials used in the calculations

Substance	δ, g/cm^3	μ, mol. weight	H, erg/g	P_m, dyne/cm^2	T_0, K	H_L, 10^{-20}, J/mol	C_2 (T_0, H_L)	$C_3(H_L)$
p-obsidian (p-obs)	2.5	67.0	7.12e10	1.07e14	2284	79.2	10.915	24928.3
Basalt (bas)	2.5	67.0	7.12e10	1.07e14	2284	79.2	10.915	24928.3
a-silicate (a-sil)	3.2	67.0	7.12e10	1.07e14	2284	79.2	10.915	24928.3
Olivine1/50 (oliv) $MgFeSiO_4$	3.3	169.1	3.21e10	6.62e14	2423	90.1	11.6969	28341.47
Olivine2/50 (op) $MgFeSiO_4$	3.3	60.1	9.60e10	3.12e11	3600	95.8	8.37068	30134.44
Pyroxene50 (p50) $Mg_{0.5}Fe_{0.5}SiO_3$	3.3	60.1	9.60e10	3.12e11	3600	95.8	8.37068	30134.44
Pyroxene100 (p100) $MgSiO_3$	3.3	60.1	9.60e10	3.12e11	3600	95.8	8.37068	30134.44

CALCULATIONS USING THE MIE THEORY

The Mie theory describes the interaction of electromagnetic waves with small-sized particles, whose characteristic scale is comparable with the wavelength. This theory allows calculating various parameters including the polarization of light and scattering indicatrix, while taking into account the wave nature of light and certain quantum effects. The main calculation formulas have the following form (Boren and Hafmen, 1983; Masafumi and Munezo, 1985):

$$Q_{\text{abs}} = Q_{\text{ext}} - Q_{\text{sca}} - \text{absorption efficiency factor.} \quad (1)$$

$$Q_{\text{pre}} = Q_{\text{ext}} - \langle\cos(\theta)\rangle Q_{\text{sca}} - \text{radiation pressure efficiency factor.} \quad (2)$$

$$Q_{\text{ext}} = \frac{2}{x^2}\sum_{n=1}^{\infty}(2n+1)\left[|a_n|^2 + |b_n|^2\right] - \text{extinction factor.} \quad (3)$$

$$Q_{\text{sca}} = \frac{2}{x^2}\sum_{n=1}^{\infty}(2n+1)\text{RE}(a_n + b_n) - \text{scatter factor.} \quad (4)$$

$$\langle\cos(\theta)\rangle = \frac{4}{x^2 Q_{\text{sca}}}\left[\sum_{n=1}^{\infty}\frac{n(n+2)}{n+1}\text{RE}(a_n a_{n+1}^* + b_n b_{n+1}^*) + \sum_{n=1}^{\infty}\frac{2n+1}{n(n+1)}\text{RE}(a_n b_n^*)\right]. \quad (5)$$

Adopted notations: $x = 2\pi s/\lambda$ is the scale parameter, where s is the radius of the particle; λ is the wavelength; θ is the scatter angle; $\langle\cos(\theta)\rangle$ is the mean effective value of $\cos(\theta)$; a_n and b_n are the internal complex parameters of summation in the Mie theory which depend on the wavelength, size of the granule, and refractive index for a given material. RE(z) is the real part of the complex number z; z^* is the complex conjugate number.

The formulas include infinite sums over a_n and b_n. These parameters are determined via the Riccati–Bessel functions, which are also written as infinite series. In practice, the summation of the series stops at a sufficiently large value $n = N_{\text{stop}}$, which allows the necessary accuracy to be achieved. As an optimal N_{stop}, Boren and Hafmen (1983) recommend taking an integer number closest to the value $N_{\text{stop}} \approx x + 4x^{1/3} + 2$, where x is the dimensionless scale parameter. The Mie theory becomes inapplicable for particles with large $x = 2\pi s/\lambda$, when the number of members in the series leads to accumulation of errors due to summation. The thermal balance and radiation pressure on the dust particles are calculated using the factors of absorption Q_{abs} and radiation pressure Q_{pre}.

The examples of calculations of these factors for basalt and olivine depending on the wavelength are given in Figs. 1–4.

It can be seen from Figs. 1–4 that the absorption and radiation pressure factors for different materials and different particle sizes vary greatly and change by several orders of magnitude depending on the wavelength.

Figures 5 and 6 separately show the absorption and radiation pressure factors for different materials and particles with a specified radius of 1 μm. The maxima at wavelengths of 10 and 20 μm, typical for the IR emission of silicates are the most distinct in Fig. 6. The same maxima with various degree of clarity are also distinct in all previous figures.

THERMAL BALANCE AND EVAPORATION OF PARTICLES

Using the kinetic theory of gases, according to (Lamy, 1974a, 1974b; Mukai and Yamamoto, 1979;

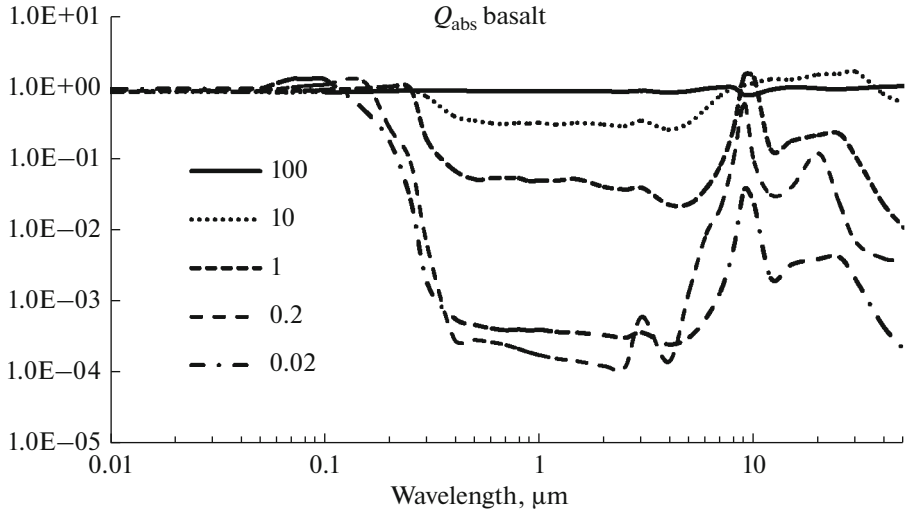

Fig. 1. Absorption factors Q_{abs} for basalt particles of different radii in micrometers.

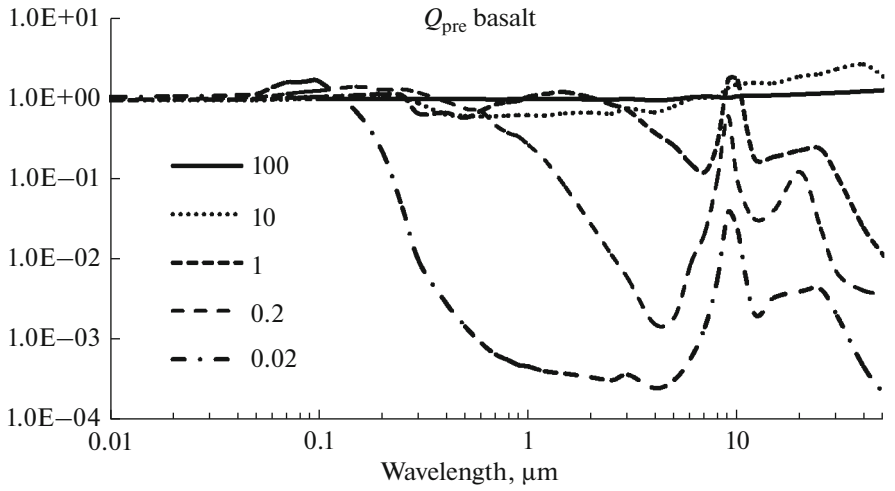

Fig. 2. Radiation pressure factors Q_{pre} for basalt particles of different radii in micrometers.

Kobayashi et al., 2011), the sublimation process can be represented in the following form:

$$\begin{aligned} ds/dt &= -P/\delta[\mu m_h/(2\pi kT)]^{1/2}, \\ P &= P_m(T)\exp[-H_L/(kT)], \text{ or} \\ P &= \exp[H_L/k\,(1/T_0 - 1/T)], \end{aligned} \tag{6}$$

where ds/dt is the rate of the radius decrease in cm/s; P is the saturated vapor pressure in torr (1 Torr = 1 mm of mercury = 133.322 Pa, 1 Pa = 10 dyne/cm^2); $P_m(T) = \exp(H_L/(kT_0))$ is the saturated vapor pressure for extremely high temperatures; δ is the density of matter in g/cm^3; μ is the molecular weight; m_h is the atomic mass unit; k is the Boltzmann constant; T is the temperature in K; H_L is the energy of evaporation of one molecule; and T_0 is the temperature at which the saturated vapor pressure $P = 1$ Torr.

Let us reduce the working formulas to the following form:

$$\begin{aligned} ds/dt &= -C_1 P/\delta(\mu/T)^{1/2} \text{ cm/s} \\ \log(P) &= C_2 - C_3/T, \end{aligned} \tag{7}$$

where C_1, C_2, and C_3 are the constants. For the constant C_1, we use the accommodation coefficient $\alpha = 0.7$ according to Lamy (1974b): $C_1 = 133.322 \times \alpha(m_h/(2\pi k))^{1/2} = 0.04083$ g/(cm s)K$^{1/2}$, therefore,

$$\frac{ds}{dt} = \frac{0.0408}{\delta} P\sqrt{\frac{\mu}{T}} \text{ cm/s}. \tag{8}$$

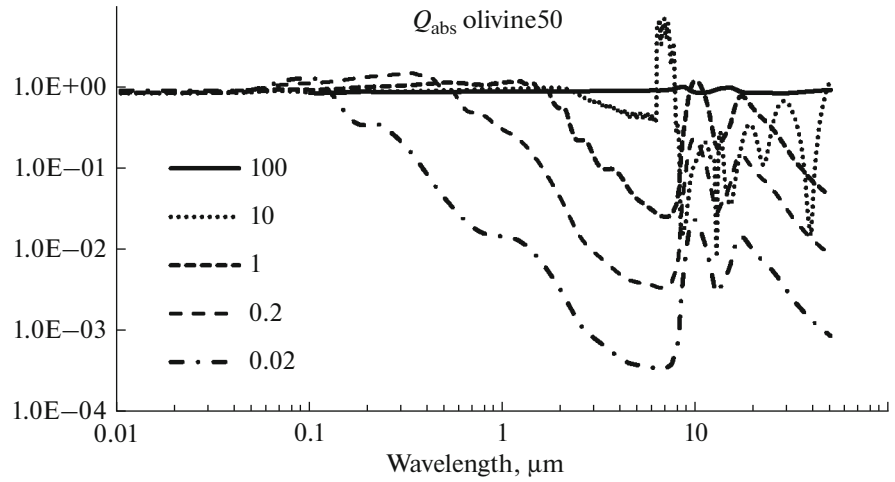

Fig. 3. Absorption factors Q_{abs} for olivine50 particles of different radii in micrometers.

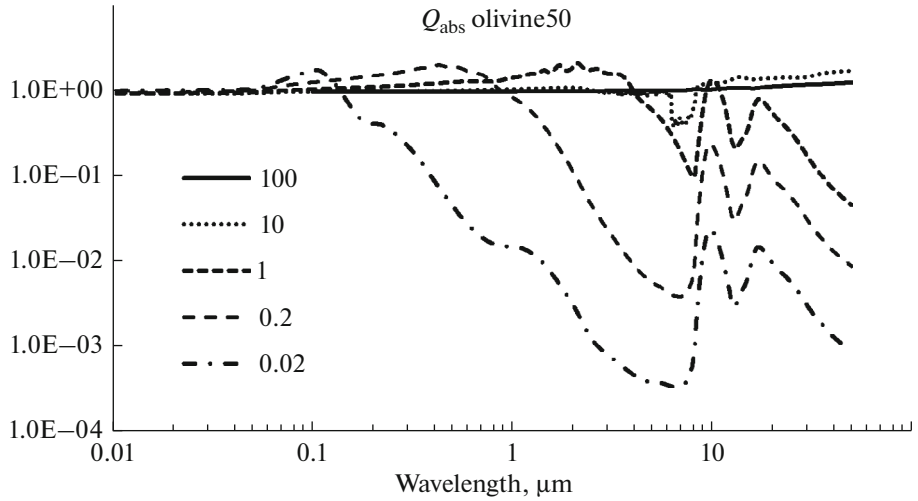

Fig. 4. Radiation pressure factors Q_{pre} for olivine50 particles of different radii in micrometers.

The value of C_1 is independent of the properties of matter, i.e., it is a universal constant. The coefficients of the second equation from (6) and (7) are the following: $C_2 = \log(e)H_L/(kT_0)$; $C_3 = \log(e)H_L/k = C_2T_0$. C_3 depends only on H_L, C_2 depends on the ratio H_L/T_0. C_2 is a dimensionless value, C_3 is measured in Kelvins.

The properties of materials are collected from the data of Lamy (1974a; 1974b; 1978) and Pollack et al. (1973) for basalt and *p*-obsidian, from Draine (1985) for the artificial substance astronomical silicate, and from Kobayashi et al. (2011) for olivine and pyroxene. All material parameters using the data from the tables of Kobayashi et al. (2011) after recalculation and addition are summarized in the Table 1.

Table 1 shows the value H, which is latent heat per unit mass or specific heat of evaporation. H (erg/g) can be easily recalculated into H_L (J/molecule) from the obvious relation: $H_L = (H \times 10^{-4})$ (μm_H) = 1.66057 × 10^{-31} μH, $P_m = 1330\exp[H_L/(kT_0)]$ dyne/cm^2, therefore $T_0 = H_L/[k\ln(P_m/1330)]$.

The material parameters of olivine1/50, which contains 50 Mg and 50% Fe, are taken in accordance with Kobayashi et al. (2011); material parameters of olivine2/50, with the same chemical composition as olivine1/50, are taken as for pyroxenes. The refractive indices correspond to the ones cited in (Dorschner et al., 1995) and coincide for olivine1/50 and olivine2/50. In the case of coinciding refractive indices, the results of calculating the absorption and radiation pressure factors based on the Mie theory and pre-

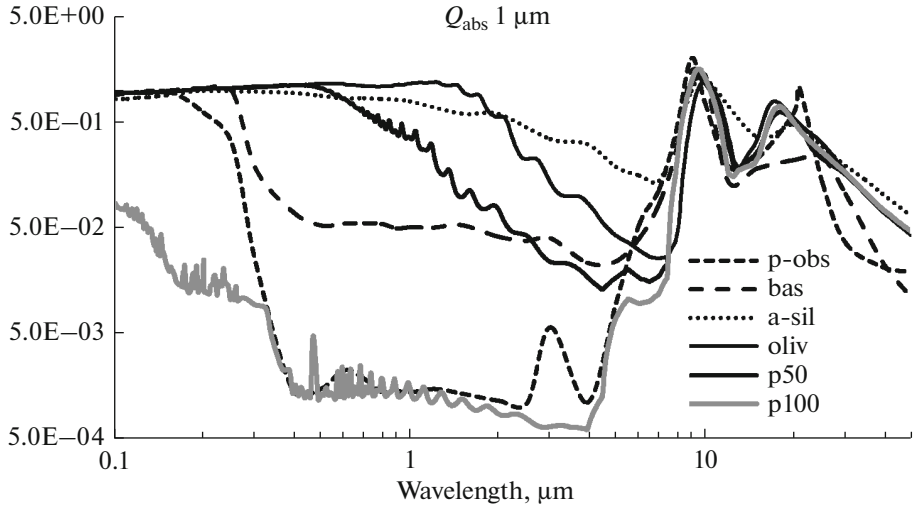

Fig. 5. Absorption factors Q_{abs} of particles with a radius of 1 μm for different materials depending on the wavelength.

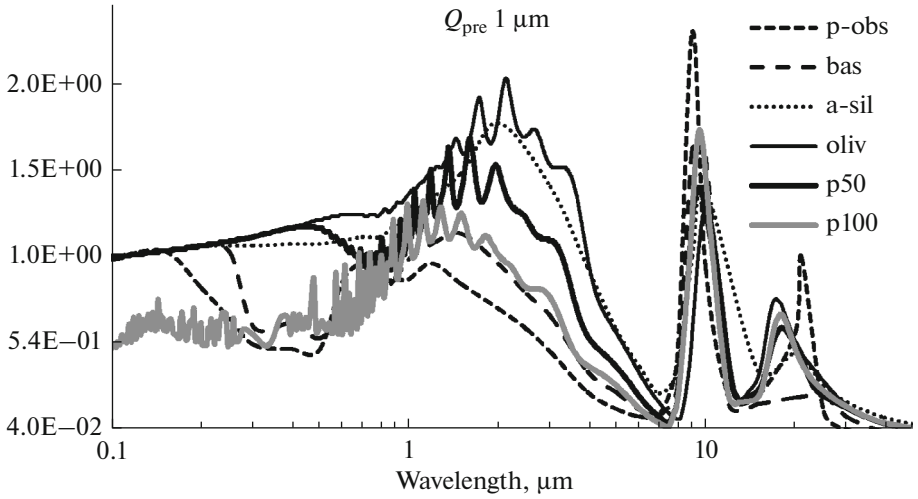

Fig. 6. Radiation pressure factors Q_{pre} of particles with a radius of 1 μm for different materials depending on the wavelength.

sented in Figs. 3–6 also coincide for olivine1/50 and olivine2/50.

In fact, we cannot determine the exact molecules that escape the dust particle during evaporation: SiO_2, whose molecular weight is close to 60, or the full molecule $MgFeSiO_4$, with the molecular weight close to 172. Obviously, such a "synthetic" molecule exists only formally and can disintegrate into other combinations of atoms before evaporation. The known data of actual measurements are still insufficient. In our opinion, the combination of SiO_2 atoms is more stable in nature; for this reason, in calculation we used the material olivine2/50.

For calculating the temperature of the dust particle, we use a natural physical requirement that, in the case of thermal equilibrium, the absorbed energy should equal the radiated energy considering the losses to evaporation:

$$E_{abs} = E_{rad} + E_{evap}, \quad (9)$$

$$E_{abs} = 2\pi s^2 \left(1 - \sqrt{1 - \frac{r_S^2}{r^2}}\right) \pi \int_{\lambda_1}^{\lambda_2} Q_{abs}(\lambda, s, m) F_S(\lambda) d\lambda, \quad (10)$$

$$E_{rad} = 4\pi s^2 \pi \int_{\lambda_1}^{\lambda_2} Q_{abs}(\lambda, s, m) B(\lambda, T) d\lambda, \quad (11)$$

where T is the temperature of the particle; $Q_{abs}(\lambda, s, m)$ is the absorption factor, which is obtained from calculations by the Mie theory and dependent on the wavelength λ, radius of the particle s, and complex refractive index of matter $m(\lambda) = n(\lambda) + ik(\lambda)$; R_s is the solar

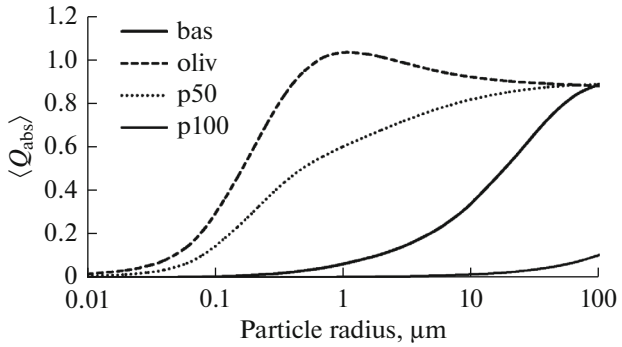

Fig. 7. Mean absorption efficiency factor $\langle Q_{abs}\rangle = \langle Q_{abs}(s, m)\rangle$ for particles of basalt (bas), olivine (oliv), pyroxen50 (p50), and pyroxen100 (p100).

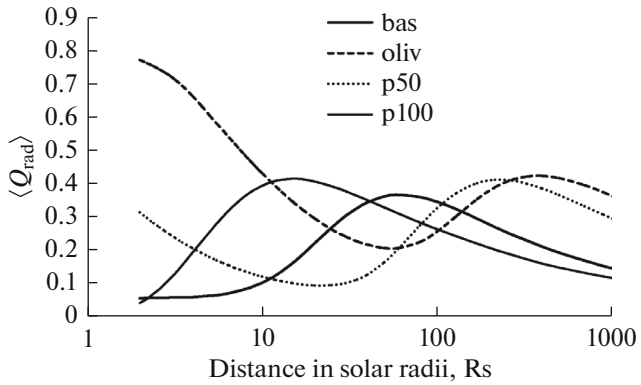

Fig. 8. Mean radiation efficiency factor $\langle Q_{rad}\rangle = \langle Q_{rad}(s,m,T)\rangle$ of dust particles with a radius of 1 μm depending on the distance to the Sun for basalt (bas), olivine (oliv), pyroxen50 (p50), and pyroxen100 (p100).

radius; R is the distance from the Sun; F_S is the distribution of energy in the solar spectrum (surface brightness); and $B(\lambda, T)$ is the Planck function. From (Mukai and Yamamoto, 1979), after transforms, we obtain:

$$E_{evap} = \frac{4\pi s^2 \delta\, ds/dt}{\mu m_H} H_L = 4\pi s^2 \frac{H_L}{m_H} C_1 P \frac{1}{\sqrt{\mu T}}, \quad (12)$$

where C_1 and P have been determined above.

Using (10)–(12), we obtain from (9) a working formula for the thermal balance equation:

$$2\pi\left(1-\sqrt{1-\frac{r_S^2}{r^2}}\right)\int_{\lambda_1}^{\lambda_2} Q_{abs}(\lambda, s, m)F_S(\lambda)d\lambda = 4\pi\int_{\lambda_1}^{\lambda_2} Q_{abs}(\lambda, s, m)B(\lambda, T)d\lambda + \frac{4C_1}{m_H}\frac{H_L P}{\sqrt{\mu T}}. \quad (13)$$

Let us introduce the following notations:

$$\langle Q_{abs}(s,m)\rangle = \frac{\int_{\lambda_1}^{\lambda_2} Q_{abs}(\lambda, s, m)F_S(\lambda)d\lambda}{\int_{\lambda_1}^{\lambda_2} F_S(\lambda)d\lambda},$$
$$\langle Q_{rad}(s,m,T)\rangle = \frac{\int_{\lambda_1}^{\lambda_2} Q_{abs}(\lambda, s, m)B(\lambda, T)d\lambda}{\int_{\lambda_1}^{\lambda_2} B(\lambda, T)d\lambda}. \quad (14)$$

The value $\langle Q_{abs}\rangle = \langle Q_{abs}(s, m)\rangle$ is the mean absorption efficiency factor, which is independent of the distance to the star (Fig. 7). The value $\langle Q_{rad}\rangle = \langle Q_{rad}(s, m, T)\rangle$ is the mean radiation efficiency factor. It depends on s, m, temperature T, and ultimately on the distance to the Sun, R. For the black body, both these factors are constant and equal to 1.

The variations in the mean radiation efficiency factor $\langle Q_{rad}\rangle$ depending on the distance to the Sun for particles of a given radius (1 μm) is illustrated in Fig. 8. Figures 9 and 10 show the changes in the parameter $\langle Q_{rad}\rangle$ depending on the particle sizes at various distances from the Sun. In Fig. 9, the distance $7R_s$ is chosen, which is close to the observed boundary of the dust-free zone (Shestakova and Demchenko, 2016), and Fig. 10 illustrates the intermediate zone, i.e., the distance of $100R_s$. Further, as the distance increases, the form of the curves remains essentially the same.

It can be seen from Fig. 7 that with increasing radius of the particles the value $\langle Q_{abs}\rangle$ tends to 1.

From Figs. 9 and 10 it can be seen that with increasing radius of the particles, $\langle Q_{rad}\rangle$, same as $\langle Q_{abs}\rangle$ (Fig. 7), tends to 1.

Let us simplify thermal balance equation (13) using introduced notations (14). Assuming the integration limits equal to $(0, \infty)$, we transform the denominators in formulas (14): $4\pi r_S^2\pi\int_0^\infty F_S(\lambda)d\lambda = L_S$ is the total solar radiation in watts; $L_S = 3.850 \times 10^{26}$ J/s. $\pi\int_0^\infty B(\lambda, T)d\lambda = \sigma T^4$ (according to the Stefan–Boltzmann law, $\sigma = 5.67032 \times 10^{-8}$ J/(s m^2 K^4)).

At large distances R, $1-\sqrt{1-\frac{r_S^2}{r^2}} = \frac{r_S^2}{2r^2}$. Then, thermal balance equation (13) can be written as follows:

$$\frac{L_S}{16\pi r^2} < \langle Q_{abs}\rangle >= \sigma T^4 \langle Q_{rad}\rangle + \frac{C_1}{m_H}\frac{H_L P}{\sqrt{\mu T}} = \sigma T^4 \langle Q_{rad}\rangle + Z(T)H_L, \quad (15)$$

where $Z(T) = \frac{C_1 P}{m_H \sqrt{\mu T}} \approx \frac{133\alpha P}{\sqrt{2\pi k T \mu m_H}}$ is the number of molecules evaporated in 1 s from 1 m^2 of the surface.

Determining the temperature from thermal balance equation (15) simplifies, if the tables of $\langle Q_{abs} \rangle$ and $\langle Q_{rad} \rangle$ are calculated in advance (Table 2). If thermal balance equation (15) is to be simplified further, the evaporation energy E_{evap} in this equation can be neglected. According to practical calculations (Figs. 11–13), the contribution of this process does not exceed several percent even near the zone of total evaporation.

Therefore, equation (15) is transformed into the following form:

$$\frac{L_S}{16\pi r^2} \langle Q_{abs} \rangle = \sigma T^4 \langle Q_{rad} \rangle. \quad (16)$$

Aside from evaporation losses, the thermal balance includes some uncertainties implied by the kinetic theory, such as the accommodation coefficient and deviation from the equilibrium state of the molecules escaping the dust particle. The uncertainty of some real parameters is also contributed by various admixtures in the chemical composition and conditionalities in deriving the calculated refractive indices for synthetic combinations of olivines and pyroxenes (Dorschner et al., 1995). The contribution of the evaporation process outside the $7R_s$ zone, according to our calculations (Figs. 11–13), does not exceed 1%, except for the olivine particles with the radii $s \le 0.1$ μm.

For comparison, the temperatures of dust granules obtained from our calculations are accompanied by similar calculations for the black body. In this case, $\langle Q_{abs} \rangle = \langle Q_{rad} \rangle = 1$. Considering that the Sun's luminosity $L_S = 4\pi R_s^2 \sigma T_{eff}$, the temperature of a dust particle can be obtained from thermal balance equation (16) depending on the distance from the Sun in the black body approximation: $T_{bb} = T_{eff} (R_s/2r)^{1/2}$.

For weakly absorbing particles, like volcanic glass and pyroxene100 (Figs. 14–15), the black body approximation is inapplicable.

Figure 16 compares the results of calculating the thermal balance equation, with and without evaporation, for olivine (as the most sensitive to this process) and pyroxene50 particles with radii of 0.1 μm. The difference in temperatures for the olivine particles becomes noticeable only at distances less than $10R_s$, and for pyroxene50, near $3R_s$. The calculations in Figs. 11–13 and 16 are performed formally up to $2R_s$, in order to demonstrate the influence of the evaporation process in the thermal balance equation. The temperatures of dust particles in this region reach extremely high values, at which they cannot remain in the solid state. Thus, it can be concluded that in real conditions, the calculation of temperature in solving

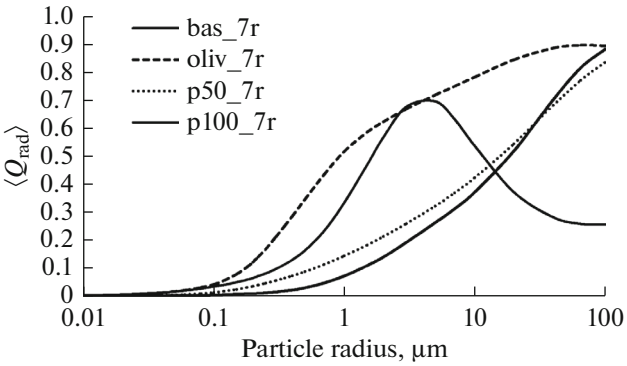

Fig. 9. Mean radiation efficiency factor $\langle Q_{rad} \rangle = \langle Q_{rad}(s, m, T) \rangle$ of dust particles at a distance of 7 R_s for basalt (bas), olivine (oliv), pyroxene50 (p50), and pyroxen100 (p100).

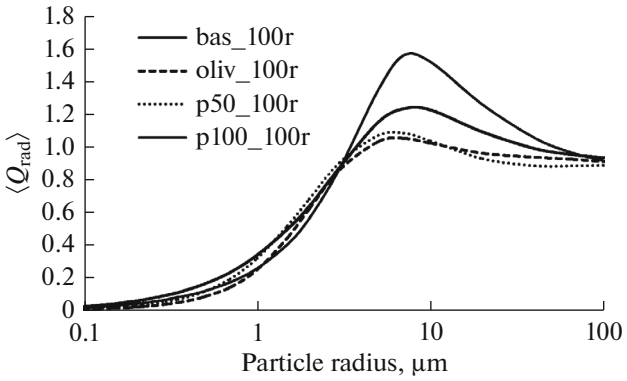

Fig. 10. Mean radiation efficiency factor $\langle Q_{rad} \rangle = \langle Q_{rad}(s, m, T) \rangle$ of dust particles at a distance of 100 R_s for basalt (bas_100r), olivine (oliv_100r), pyroxene50 (p50_100r), and pyroxene100 (p100_100r).

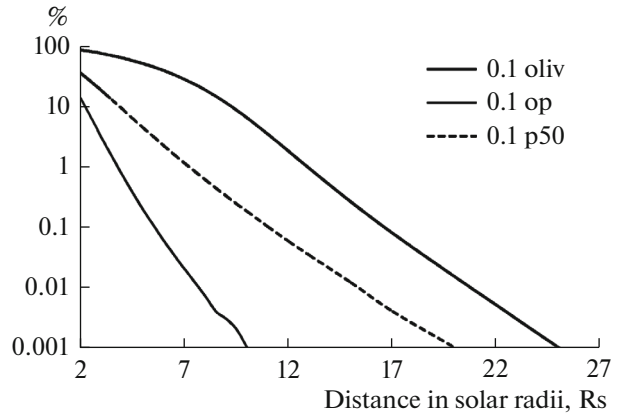

Fig. 11. Percent contribution of the evaporation process in the thermal balance equation for the particles of different materials with a radius of 0.1 μm depending on the distance to the Sun.

Table 2. $\langle Q_{abs} \rangle$ for basalt particles of different sizes (s) and $\langle Q_{rad} \rangle$ for the range of distances from $7R_s$ to Jupiter ($1119R_s$)

s	$\langle Q_{abs} \rangle$	$\langle Q_{rad} \rangle$													
μm		7.0 R_s	8.0 R_s	9.0 R_s	10.0 R_s	12.0 R_s	15.0 R_s	20.0 R_s	30.0 R_s	40.0 R_s	60.0 R_s	100 R_s	215 R_s	500 R_s	1119 R_s
0.04	0.0015	0.003	0.003	0.004	0.005	0.006	0.008	0.010	0.013	0.014	0.014	0.012	0.009	0.006	0.005
0.06	0.0026	0.004	0.004	0.005	0.006	0.008	0.011	0.015	0.019	0.021	0.021	0.019	0.014	0.010	0.007
0.08	0.0037	0.004	0.005	0.007	0.008	0.010	0.014	0.019	0.025	0.027	0.028	0.025	0.019	0.013	0.010
0.10	0.0050	0.005	0.007	0.008	0.009	0.012	0.017	0.023	0.031	0.034	0.035	0.032	0.024	0.017	0.012
0.15	0.0084	0.008	0.009	0.011	0.013	0.017	0.023	0.033	0.045	0.050	0.052	0.048	0.037	0.026	0.019
0.18	0.0106	0.009	0.011	0.013	0.015	0.020	0.027	0.039	0.053	0.060	0.063	0.059	0.045	0.032	0.023
0.20	0.0120	0.010	0.012	0.014	0.016	0.022	0.030	0.042	0.059	0.067	0.070	0.065	0.050	0.036	0.026
0.25	0.0156	0.013	0.015	0.018	0.020	0.027	0.037	0.052	0.073	0.083	0.088	0.082	0.063	0.045	0.032
0.30	0.0191	0.016	0.019	0.022	0.025	0.032	0.044	0.063	0.088	0.100	0.106	0.099	0.077	0.054	0.039
0.40	0.0261	0.023	0.026	0.030	0.034	0.043	0.059	0.084	0.117	0.134	0.143	0.134	0.103	0.073	0.053
0.50	0.0328	0.031	0.035	0.039	0.044	0.056	0.075	0.106	0.148	0.169	0.180	0.169	0.130	0.092	0.066
0.70	0.0458	0.048	0.053	0.060	0.067	0.083	0.109	0.151	0.210	0.239	0.255	0.239	0.185	0.131	0.094
1	0.0634	0.073	0.081	0.090	0.100	0.123	0.160	0.219	0.301	0.342	0.365	0.344	0.268	0.191	0.138
1.5	0.0879	0.110	0.121	0.133	0.147	0.177	0.226	0.305	0.419	0.480	0.520	0.501	0.404	0.295	0.214
2	0.1088	0.141	0.154	0.169	0.184	0.219	0.275	0.367	0.506	0.586	0.647	0.641	0.539	0.408	0.298
3	0.1455	0.193	0.208	0.225	0.243	0.281	0.344	0.450	0.624	0.736	0.842	0.878	0.798	0.641	0.482
5	0.2092	0.264	0.281	0.299	0.319	0.359	0.423	0.533	0.726	0.868	1.034	1.153	1.167	1.045	0.859
7	0.2656	0.313	0.330	0.348	0.366	0.405	0.466	0.568	0.753	0.895	1.077	1.234	1.321	1.272	1.139
10	0.3398	0.372	0.388	0.404	0.420	0.455	0.508	0.597	0.759	0.888	1.060	1.227	1.356	1.376	1.312
20	0.5250	0.520	0.531	0.542	0.553	0.575	0.610	0.666	0.768	0.852	0.969	1.093	1.210	1.277	1.302
40	0.7281	0.703	0.709	0.715	0.720	0.732	0.750	0.779	0.829	0.870	0.929	0.992	1.055	1.100	1.124
100	0.8876	0.884	0.886	0.887	0.889	0.893	0.897	0.903	0.912	0.919	0.927	0.935	0.946	0.964	0.980

the thermal balance equation can be performed without account for the evaporation process.

Figure 14 presents the results of calculations of the particle temperature at the distance of $10r_s$ depending on their radii s. Figure 15 shows the variations in temperature depending on the distance from the Sun for the particles with radius 1 μm. It is shown that the temperatures of particles of different size and material differ from each other and from the black body.

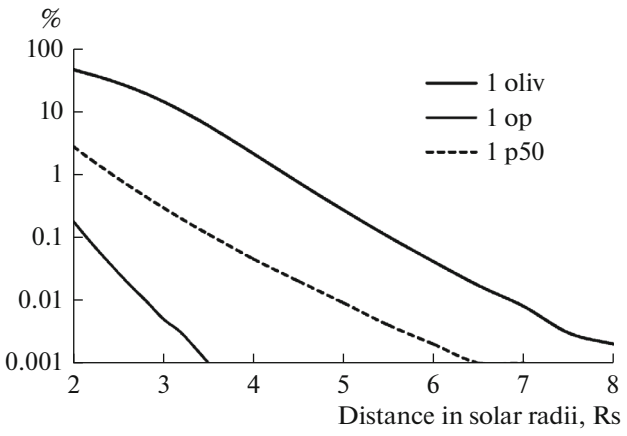

Fig. 12. Percent contribution of the evaporation process in the thermal balance equation for the particles of different materials with a radius of 1 μm depending on the distance to the Sun.

Surprisingly, the temperatures of olivine, pyroxen50, and astrosilicate particles can exceed the black body temperature (Figs. 14 and 15). Such results are the consequence of the wave nature of light, when the effective cross-section of the particles exceeds geometric parameters. With an increase in particle dimensions, the temperatures tend to that of the black body, the diffraction effects decrease, and the cross-section of particles can be brought to geometric optics, i.e., to the trivial value of the cross-section area: πs^2.

CALCULATIONS OF RADIATION PRESSURE

The calculation of the mean radiation factor $Q_{pr} = \langle Q_{pre} \rangle$ and ratio of the radiation pressure to the gravitational force $\beta = F_{pre}/F_{grav}$ was performed depending on the material and radius of the dust particle. These parameters are independent of the distance to the Sun.

The formulas have the form:

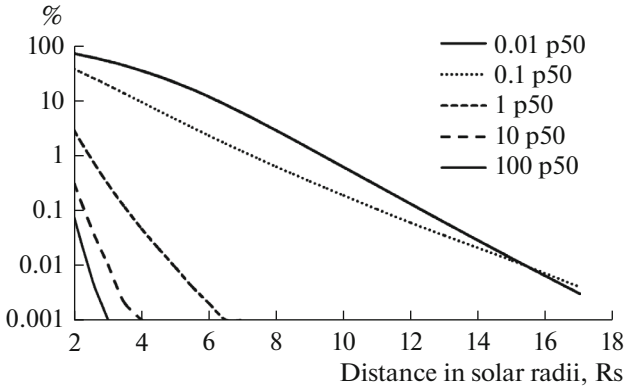

Fig. 13. Percent contribution of the evaporation process in the thermal balance equation for the pyroxene50 particles with different radii (shown in μm) depending on the distance to the Sun.

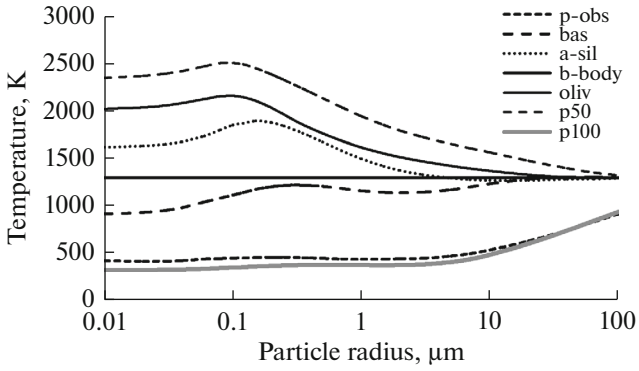

Fig. 14. Temperature of particles of various materials at a distance of $10R_S$ depending on the particle radius.

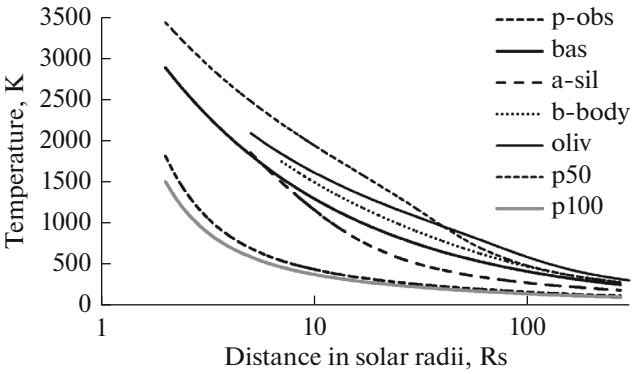

Fig. 15. Temperature of particles of different materials with radii of 1 μm depending on the distance to the Sun.

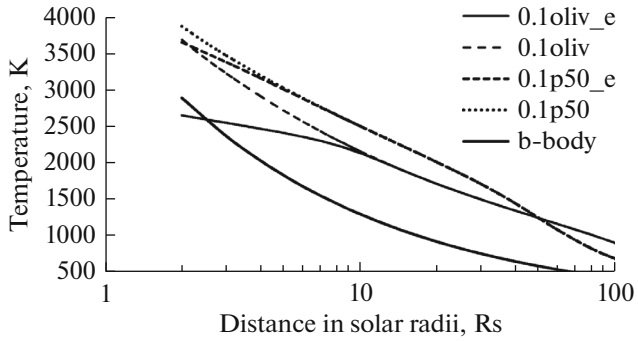

Fig. 16. Comparison of temperature calculations for particles with a radius of 0.1 μm performed considering the evaporation process in the thermal balance equation (0.1oliv_e, 0.1p50_e) and without evaporation (0.1oliv, 0.1 p50); b-body is the black body.

$$Q_{\rm pr}(s,m)=\frac{\int_{\lambda_1}^{\lambda_2}Q_{\rm pre}(\lambda,s,m)F_S(\lambda)d\lambda}{\int_{\lambda_1}^{\lambda_2}F_S(\lambda)d\lambda},$$
$$\beta(s,m)=\frac{F_{\rm pre}}{F_{\rm grav}}=\frac{3Q_{\rm pr}(s,m)L_S}{16\pi c\mu_s\delta s}, \quad (17)$$

where $Q_{\rm pre}(\lambda, s, m)$ is the spectral efficiency factor for the radiation pressure calculated by the Mie theory; $m = n + ik$ is the complex refractive index; $F_S(\lambda)$ is the solar radiation flux; L_S is the total solar luminosity; $\mu_s = GM_S$ is the solar gravitational parameter; G is the gravitational constant; M_S is the solar mass; c is the velocity of light; and δ is the density of matter in the dust particle.

As can be seen from Fig. 17, the maximum radiation pressure occurs in particles with radii of approximately 0.2 μm, which are affected more strongly by the solar radiation than the others. Due to the influence of the radiation pressure, the particles of olivine50, astrosilicate, and pyroxene50, for which the β value in the size interval 0.1–0.3 μm is close to 1, can escape the Solar System more easily than the others. More real materials, whose refractive indexes are obtained not from compilation and calculations, but from laboratory measurements, such as basalt and p-obsidian, as well as 100% pyroxene, are less affected by the radiation pressure (Fig. 17).

ALGORITHM FOR CALCULATING THE ORBITAL EVOLUTION

The calculation of the orbital evolution of the dust particles is based on the numerical integration of the system of three differential equations:

$$\frac{d^2r}{dt^2}=r\left(\frac{d\varphi}{dt}\right)^2-\frac{\mu}{r^2}\left(1-\beta-\beta'\frac{V_{wr}-dr/dt}{U}\right), \quad (18)$$

$$\frac{d^2\varphi}{dt^2}=-\frac{1}{r^2}\left[2r\frac{dr}{dt}\frac{d\varphi}{dt}+\alpha\frac{d\varphi}{dt}\left(1+\frac{r_s^2}{2r^2}\right)+\alpha'\left(\frac{d\varphi}{dt}-\frac{V_{w\tau}}{r}\right)\right], \quad (19)$$

where the third equation is (8), which determines the evaporation rate of the particle, ds/dt.

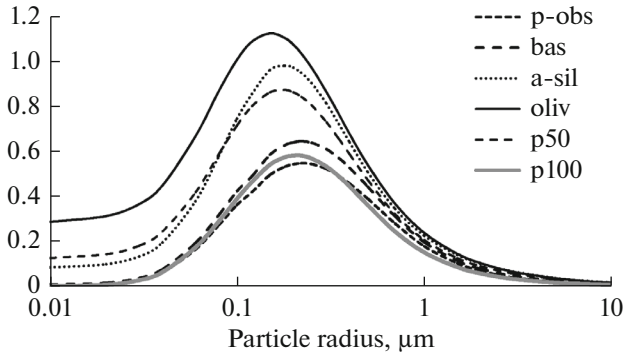

Fig. 17. Ratio of radiation pressure to gravitational force depending on the radius of the particles for various materials.

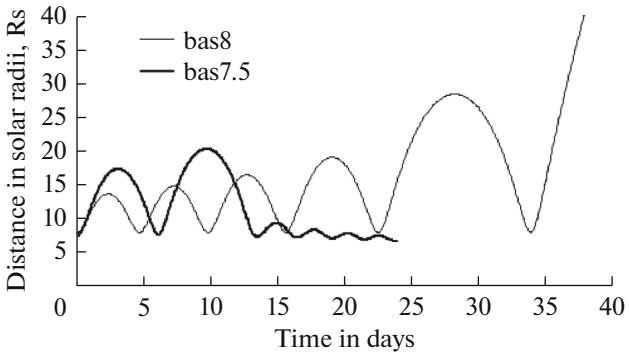

Fig. 18. Orbital evolution of basalt particles with a radius of 1 μm; starting distances are $8R_S$ and $7.5R_S$.

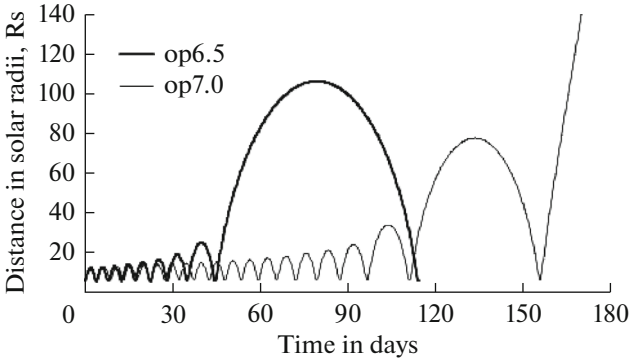

Fig. 19. Orbital evolution of olivine2/50 particles with a radius of 1 μm with pyroxene parameters; starting distances are 7.0 R_S and 6.5 R_S.

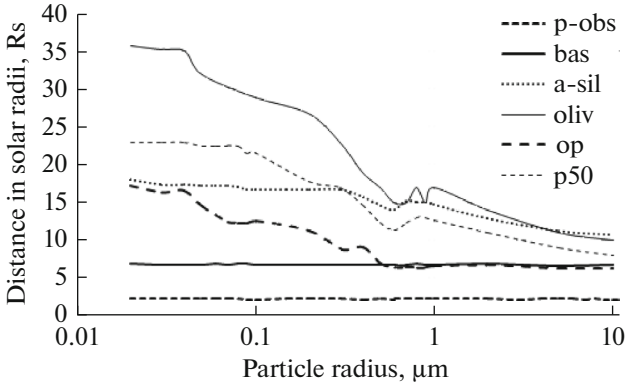

Fig. 20. Boundaries of the sublimation zone for the dust particles of different materials.

The saturated vapor pressure P is calculated by the formula $\log(P) = C_2 - C_3/T$, with coefficients C_2 and C_3 listed in Table 1, where P is expressed in torr. If the pressure P is expressed in torr, and the density of the substance δ in g/cm^3, then the rate of decrease of the particle's radius ds/dt will have the dimensions of cm/s.

The following notations are adopted: R is the distance to the Sun; φ is the polar angle (angle of rotation of the vector **r**); $\beta' = \dfrac{3\dot{M}_S U^2}{16\pi\mu s\delta V_{wr}}$ is analogous to β, i.e., the ratio of the solar wind pressure to the gravity; $\dot{M}_S$ and r_s are the mass loss and radius of the Sun; V_{wr} and $V_{w\tau}$ are the radial and tangential components of the solar wind velocity; $\alpha = \beta\mu/s$; $\alpha' = \beta'\mu/U$; and $U = \sqrt{V_{wr}^2 + V_{w\tau}^2}$ is the magnitude of the solar wind velocity.

The set of Eqs. (8), (18), and (19) is equivalent to the system of five first-order differential equations with respect to the sought time functions: $r, \dot{r}, \varphi, \dot{\varphi}, s$. This system is solved using the fourth-order Runge–Kutta method with a constant step size.

The starting conditions are specified separately: the particles either move autonomously with a circular orbital velocity, or escape from the parent bodies (comets) with a parabolic velocity.

RESULTS OF CALCULATING THE ORBITAL EVOLUTION

The orbital evolution of particles depends on the starting distance and initial radius of the particles, since the sublimation rate depends on the temperature, which, in turn, strongly depends on the initial parameters. Figures 18 and 19 show the examples of the orbital evolution of the particles that start from the circular orbits. The calculations have shown (Figs. 18, 19) that a particle with an initial radius of 1.0 μm gradually approaches the Sun and "spirals in" as a result of the combined influence of the Poynting–Robertson drag force from the radiation pressure and solar wind. Depending on the starting distance, the final behavior of particles differs.

The common feature in the behavior of particles of all materials is the starting distance that acts as a bifurcation point (Tables 3, 4). Close to this distance, an

Table 3. Boundaries of total evaporation (R_o) and starting distances (R_{start}) for the particles with different radii (s), limiting the region of bifurcation of the final behavior of particles

	p-obsidian			basalt			olivine1/50		
s, μm	R_o(R_s) evaporation	R_{start} fall	R_{start} escape	R_o(R_s) evaporation	R_{start} fall	R_{start} escape	R_o(R_s) evaporation	R_{start} fall	R_{start} escape
0.02	2.36	Fall from any distance		7	Fall from any distance		35.8	Fall from any distance	
0.03	2.33			6.84			35.24		
0.04	2.33			6.81			35		
0.05	2.29			6.81			32	33	34
0.06	2.25			6.9			–	–	–
0.07	2.2			6.84			–	–	–
0.08	2.22			6.9			–	–	–
0.09	2.20			6.86			–	–	–
0.1	2.18			6.84			29	30	31
0.15	2.23	3	3.1	6.77	11.30	8.5	–	–	–
0.2	2.25	2.5	2.6	6.76	8.87	8	26.84	28	29
0.3	2.28	2.4	2.5	6.78	9.09	8	23	23	24
0.4	2.21	2.4	2.5	6.84	6.89	8	19	19	20
0.5	2.3	2.3	2.4	6.83	6.38	8	17	17	18
0.6	2.22	2.4	2.5	6.76	6.39	8	15	15	16
0.7	2.36	2.5	2.6	6.71	6.38	8	15	15	16
0.8	2.25	2.4	2.5	7	6.40	7.5	17	17	18
0.9	2.26	2.4	2.5	6.8	6.67	8	15	15	16
1	2.24	2.5	2.6	6.8	6.78	8	17	Fall from any distance	
2	2.22	2.7	2.8	6.9	6.36	8	14		
5	2.22	Fall from any distance		6.6	7	7.5	11		
10	2.20			6.7	7	7.5	10		
Average	2.2			6.8			21.6		

initially circular orbit of the particle becomes more elongated with each pass, and the particle either leaves the Solar System in the state of partial evaporation, or falls on the Sun and evaporates completely.

The final stage of evaporation determines the boundary of the dust-free zone, near which the particles of all sizes of the given material evaporate. The boundary of the dust-free zone (R_o) is different for each material, as illustrated by Figs. 18 and 19 and listed in Tables 3 and 4. Tables 3 and 4 also show the pairs of close starting distances (R_{start}), between which there is a bifurcation point, which determines the final split in the behavior of the particle: fall on the Sun and total evaporation or escape from the near-solar region in a state of partial evaporation.

As can be seen from Fig. 20 and Tables 3 and 4, the evaporation zone for particles of various chemical composition covers the distances from $2.2R_s$ for iron-poor p-obsidian to $35R_s$ for iron-containing olivine.

For some materials, such as p-obsidian and basalt, the boundary of the dust-free zone is independent of particle sizes and, on average, is at the distance $2.2R_s$ and $6.8R_s$ respectively. Other materials show that the particles with small initial size evaporate at greater distances from the Sun. Further, with increasing starting sizes of particles, the radius of the boundary of the dust-free zone stabilizes. For example, material olivine2/50 with the parameters of pyroxene, conventionally denoted in the figures by "op", for the particles with initial radius $s \geq 0.5$ μm shows the average distance of evaporation $6.5R_s$, which is close to the evaporation zone of basalt (Fig. 20). Large particles with a radius of approximately 10 μm, typical for the zodiacal

Table 4. Boundaries of total evaporation (R_o) and starting distances (R_{start}) for the particles with different radii (s), limiting the region of bifurcation of the final behavior of particles

	olivine2/50 with pyroxene parameters			pyroxene50			astron. silicate		
s, μm	$R_o(R_s)$ evaporation	R_{start} fall	R_{start} escape	$R_o(R_s)$ evaporation	R_{start} fall	R_{start} escape	$R_o(R_s)$ evaporation	R_{start} fall	R_{start} escape
0.02	17.3	Fall from any distance		23	Fall from any distance		18	Fall from any distance	
0.03	16.38			23			17.4		
0.04	16.64			23			17.4		
0.05	14.578	15	16	22.5			17.3		
0.06	13.47	14	15	22.5			17.2		
0.07	12.41	13	14	22.5			17.2		
0.08	12.32	13	14	22.4	24	25	17	19	20
0.09	12.218	13	14	21.5	23	24	16.8	18	19
0.1	12.524	12	13	21.7	23	24	16.8	18	19
0.2	11.303	11	12	17.8	20	21	16.7	18	19
0.3	8.868	8.5	9	17	16	17	16.7	18	19
0.4	9.086	7.5	8	14.7	14	15	15.8	17	19
0.5	6.888	6.5	7	12.3	12	13	14.5	16	18
0.6	6.382	6	6.2	11.3	11	12	14.1	14	17
0.7	6.385	6.2	6.5	12.3	11	12	15.2	15	15
0.8	6.378	6.2	6.5	13	13	14	15.1	15	16
0.9	6.4	6	6.2	13	13	14	15.1	15	16
1	6.67	6.5	7	12.6	12	13	14.8	Fall from any distance	
2	6.78	Fall from any distance		11	Fall from any distance		12.9		
5	6.36			9			11.2		
10	6.33			8			10.8		
Average	10.3			16.9			15.7		

cloud, for all materials in consideration, evaporate inside the zone of $11R_s$.

From the results of calculations of thermal balance, it has been shown that the temperatures of particles of different sizes and materials differ from each other and from a black body. The maximum radiation pressure occurs in particles with a radius of approximately 0.2 μm. The particles with sizes smaller than 0.2 μm approach the Sun in a spiral, in accordance with the Poynting–Robertson law, without exiting to highly elliptical orbits. Under the influence of radiation pressure, the particles of olivine50, astrosilicate, and pyroxene50 escape the Solar System more easily than the others, while such materials as basalt, p-obsidian, and pyroxen100 are less affected by the radiation pressure (Fig. 17).

The particles from the comet bodies, i.e., those that move in parabolic orbits, leave the Solar System regardless of their size. Due to the influence of the radiation pressure, their orbits become hyperbolic (Fig. 17).

The particles of basalt and "hybrid" olivine ($MgFeSiO_4$) with material parameters of pyroxene are in better agreement with the observations (Shestakova and Demchenko, 2016) than the others. The considerable advantage of basalt is the reliable initial data on the refractive indices obtained from laboratory measurements (Lamy, 1978; Pollack et al., 1973), unlike the refractive index data acquired by calculations and compilations (Draine, 1985; Dorschner et al., 1995).

ACKNOWLEDGMENTS

The work is supported by the Targeted Financing Program BR05336383 Aerospace Committee of the Ministry of Defense and Aerospace Industry of the Republic of Kazakhstan.

REFERENCES

Aimanov, A.K., Aimanova, G.K., and Shestakova, L.I., Radial velocities in the F-corona on July 11, 1991, *Astron. Lett.*, 1995, vol. 21, no. 2, pp. 196–198.

Beavers, W.I. and Eitter, J.J., Radial velocity discriminated coronal photometric measurements at the July 11, 1991 total eclipse, *Planet. Space Sci.*, 2009, vol. 57, pp. 332–343.

Belton, M.J.S., Dynamics of interplanetary dust, *Science*, 1966, vol. 151, pp. 35–44.

Blackwell, D.E., A study of the outer corona from a high altitude aircraft at the eclipse of 1954 June 30. I. Observational data, *Mon. Not. R. Astron. Soc.*, 1955, vol. 115, pp. 629.

Boren, C.F. and Hafmen, D.R., *Absorption and Scattering of Light by Small Particles*, New York: Wiley, 1983.

Burns, J.A., Lamy, P.L., and Soter, S., Radiation forces on small particles in the Solar system, *Icarus*, 1979, vol. 40, pp. 1–48.

Dorschner, J., Begemann, B., Henning, Th., Jager, C., and Mutschke, H., Steps toward interstellar silicate mineralogy II. Study of Mg–Fe-silicate glasses of variable composition, *Astron. Astrophys.*, 1995, vol. 300, pp. 503–520.

Draine, B.T., Tabulated optical properties of graphite and silicate grains, *Astrophys. J.*, 1985, vol. 57, suppl., pp. 587–594.

Hodapp, K.-W., MacQueen, R.M., and Hall, D.N.B., A search during the 1991 solar eclipse for the infrared signature of circumsolar dust, *Nature*, 1992, vol. 355, pp. 707–710.

Ingham, M.F., The nature and distribution of the interplanetary dust, *Mon. Not. R. Astron. Soc.*, 1961, vol. 122, pp. 157–176.

Kaiser, C.B., The thermal emission of the F Corona, *Astrophys. J.*, 1970, vol. 159, pp. 77–92.

Kelsall, T., Weiland, J.L., Franz, B.A. Reach, W.T., Arendt, R.G., Dwek, E., Freudenreich, H.T., Hauser, M.G., Moseley, S.H., and Odegard, N.P., The COBE diffuse infrared background experiment search for the cosmic infrared background. II. Model of the interplanetary dust cloud, *Astrophys. J.*, 1998, vol. 508, pp. 44–73.

Kobayashi, H., Kimura, H., Watanabe, S., Yamamoto, T., and Müller, S., Sublimation temperature of circumstellar dust particles and its importance for dust ring formation, *Earth, Planets Space*, 2011, vol. 63, pp. 1067–1075.

Lamy, P.L., The dynamics of circum-solar dust grains, *Astron. Astrophys.*, 1974a, vol. 33, pp. 191–194.

Lamy, P.L., Interaction of interplanetary dust grains with the solar radiation field, *Astron. Astrophys.*, 1974b, vol. 35, pp. 197–207.

Lamy, P.L., Optical properties of silicates in the far ultraviolet, *Icarus*, 1978, vol. 34, pp. 68–75.

Lamy, P.L., Kuhn, J.R., Lin, H., Koutchmy, S., and Smartt, R.N., No evidence of a circumsolar dust ring from infrared observations of the 1991 solar eclipse, *Science*, 1992, vol. 257, pp. 1377–1380.

Leinert, C., Zodiacal light—a measure of the interplanetary environment, *Space Sci. Rev.*, 1975, vol. 18, pp. 281–339.

Lena, P., Hall, D., Soufflot, A., and Viala, Y., The thermal emission of the dust corona, during the eclipse of June 30, 1973. II–Photometric and spectral observations, *Astron. Astrophys.*, 1974, vol. 37, pp. 81–86.

MacQween, R.M., Infrared observation of the outer solar corona, *Astrophys. J.*, 1968, vol. 154, pp. 1059–1076.

Makarov, E.A., Kharitonov, A.V., and Kazachevskaya, T.V., *Potok solnechnogo izlucheniya (The Flux of Solar Radiation)*, Moscow: Nauka, 1991.

Mann, I. and MacQueen, R.M., The solar F-corona at 2.12 pin: calculations of near-solar dust in comparison to 1991 eclipse observations, *Astron. Astrophys.*, 1993, vol. 275, pp. 293–297.

Masafumi, M. and Munezo, S., Polarization efficiency and phase function, calculated on the basis of the Mie theory, *Sci. Rep. Tohoku Univ., Ser. 8*, 1985, vol. 6, no. 1, pp. 11–48.

Mukai, T. and Yamamoto, T., A model of the circumsolar dust cloud, *Publ. Astron. Soc. Jpn.*, 1979, vol. 31, pp. 585–596.

Mukai, T., Yamamoto, T., Hasegawa, A. Fujiwara, A., and Koike, C., On the circumsolar grain materials, *Publ. Astron. Soc. Jpn.*, 1974, vol. 26, pp. 445–458.

Pollack, J.B., Toon, O.B., and Khare, B.N., Optical properties of some terrestrial rocks and glasses, *Icarus*, 1973, vol. 19, pp. 372–389.

Peterson, A.W., Experimental detection of thermal radiation from interplanetary dust, *Astrophys. J.*, 1967, vol. 148, pp. L37–L39.

Reach, W.T., Franz, B.A., and Weiland, J.L., The three-dimensional structure of the zodiacal dust bands, *Icarus*, 1997, vol. 127, pp. 461–484.

Roser, S. and Staude, H.J., The Zodiacal light from 1500 Å to 60 micron, *Astron. Astrophys.*, 1978, vol. 67, pp. 381–394.

Shcheglov, P.V., Shestakova, L.I., and Ajmanov, A.K., Results of interferometric observations of the F-corona radial velocity field between 3 and 7 solar radii, *Astron. Astrophys.*, 1987, vol. 173, pp. 383–388.

Shestakova, L.I., Interpretation of F-corona radial velocity observations, *Astron. Astrophys.*, 1987, vol. 175, pp. 289–291.

Shestakova, L.I. and Demchenko, B.I., Results of observations of the dust distribution in the F-corona of the Sun, *Sol. Syst. Res.*, 2016, vol. 50, no. 2, pp. 143–160.

Shestakova, L.I. and Tambovtseva, L.V., Dynamics of dust grains near the Sun, *Astron. Astrophys.*, 1995, vol. 8, pp. 59–81.

Shestakova, L.I., Rspaev, F.K., Minasyants, G.S., and Dubovitskij, A.I., The observation of total solar eclipse on March 29, 2006 in Kazakhstan, *Odessa Astron. Publ.*, 2007, vol. 20, pp. 203–204.

Shestakova, L.I., Demchenko, B.I., Rspaev, F.K., Minasyants, G.S., and Dubovitskii, A.I., Observation of the radial velocities of dust in the F-corona during a total solar eclipse on August 1, 2008, *Izv. Akad. Nauk Resp. Kazakh., Ser. Fiz.-Matem.*, 2009, no. 4, pp. 97–104.

Veselovskii, I.S., Solar wind and heliospheric magnetic field, in *Model' kosmosa. Tom 1. Fizicheskie usloviya v kosmicheskom prostranstve* (Space Model, Vol. 1: Physical Conditions in the Space), Panasyuk, M.I. and Novikov, L.S., Eds., Moscow: Universitet, 2007, pp. 314–359.

Translated by M. Chubarova